



EEG microstate periodicity explained by rotating phase patterns of resting-state alpha oscillations

F. von Wegner^{a,b,*}, S. Bauer^b, F. Rosenow^b, J. Triesch^c, H. Laufs^d

^a School of Medical Sciences, University of New South Wales, Wallace Wurth Building, Kensington, NSW 2052, Australia

^b Epilepsy Center Frankfurt Rhine-Main, Center of Neurology and Neurosurgery, University Hospital Frankfurt and Center for Personalized Translational Epilepsy Research (CePTER), Goethe University Frankfurt, Frankfurt am Main, Germany

^c Frankfurt Institute for Advanced Studies (FIAS), Frankfurt am Main, Germany

^d Department of Neurology, Christian-Albrechts University Kiel, Arnold-Heller-Strasse 3, Kiel 24105, Germany

ARTICLE INFO

Keywords:

EEG
Resting-state
Alpha oscillations
Microstates
Phase rotors

ABSTRACT

Spatio-temporal patterns in electroencephalography (EEG) can be described by microstate analysis, a discrete approximation of the continuous electric field patterns produced by the cerebral cortex. Resting-state EEG microstates are largely determined by alpha frequencies (8–12 Hz) and we recently demonstrated that microstates occur periodically with twice the alpha frequency.

To understand the origin of microstate periodicity, we analyzed the analytic amplitude and the analytic phase of resting-state alpha oscillations independently. In continuous EEG data we found rotating phase patterns organized around a small number of phase singularities which varied in number and location. The spatial rotation of phase patterns occurred with the underlying alpha frequency. Phase rotors coincided with periodic microstate motifs involving the four canonical microstate maps. The analytic amplitude showed no oscillatory behaviour and was almost static across time intervals of 1–2 alpha cycles, resulting in the global pattern of a standing wave.

In $n=23$ healthy adults, time-lagged mutual information analysis of microstate sequences derived from amplitude and phase signals of awake eyes-closed EEG records showed that only the phase component contributed to the periodicity of microstate sequences. Phase sequences showed mutual information peaks at multiples of 50 ms and the group average had a main peak at 100 ms (10 Hz), whereas amplitude sequences had a slow and monotonous information decay. This result was confirmed by an independent approach combining temporal principal component analysis (tPCA) and autocorrelation analysis.

We reproduced our observations in a generic model of EEG oscillations composed of coupled non-linear oscillators (Stuart-Landau model). Phase-amplitude dynamics similar to experimental EEG occurred when the oscillators underwent a supercritical Hopf bifurcation, a common feature of many computational models of the alpha rhythm.

These findings explain our previous description of periodic microstate recurrence and its relation to the time scale of alpha oscillations. Moreover, our results corroborate the predictions of computational models and connect experimentally observed EEG patterns to properties of critical oscillator networks.

1. Introduction

The electrical activity of the cerebral cortex is a regular but highly complex spatio-temporal process that results from spontaneous neuronal oscillations and is further shaped by extensive intra-cortical connections, cortico-subcortical feedback loops as well as external input. Temporal patterns are characterized by oscillations in the now classical frequency bands that approximately spread the 0–100 Hz frequency range, although higher frequencies occur (Schomer and da Silva, 2011). The

spatial patterns formed by task-free spontaneous activity mostly lack a uniform description, though stimulus-induced patterns are well understood in the context of numerous experimental paradigms such as event-related potentials (Freeman, 2004a; 2004b; Murray et al., 2008). A prominent approach to characterize spatial patterns recorded by surface electroencephalography (EEG) is the microstate algorithm, used in both task-related and task-free EEG (Koenig et al., 2002; Lehmann et al., 1987; Murray et al., 2008). When using this clustering technique, typically four representative topographies (microstates) of the surface

* Corresponding author at: School of Medical Sciences, University of New South Wales, Wallace Wurth Building, Kensington, NSW 2052, Australia.
E-mail address: f.vonwegner@unsw.edu.au (F. von Wegner).

electrical potential are sufficient to explain approximately 70% of the variance of resting-state EEG data sets (von Wegner et al., 2018). EEG time series can thus be represented by a sequence of labels taken from a small alphabet such as (A, B, C, D). Despite the massive compression ratio during the transition from the set of all possible EEG topographies to a set of only four microstate maps, microstates have been proven to convey valid information about the vigilance state (Brodbeck et al., 2012), functional brain states (Britz et al., 2010; Musso et al., 2010; Yuan et al., 2012), different classes of cognitive processes (Milz et al., 2015; Zappasodi et al., 2019), and increasingly about anomalies in neuro-psychiatric diseases (Lehmann et al., 2005; Murphy et al., 2020; Musaeus et al., 2019; Nishida et al., 2013; Smailovic et al., 2019). Analytic strategies include a classification of the microstate map geometries revealed by the given clustering algorithm (Koenig et al., 1999; Kuhn et al., 2015; Smailovic et al., 2019), as well as a characterization of the temporal dynamics within the microstate sequences. Temporal properties of microstate sequences have been described by transition probability matrices, i.e. by Markov chain models (Kuhn et al., 2015; Lehmann et al., 2005; Musaeus et al., 2019; Nishida et al., 2013; Schiller et al., 2019), but also as random walks with memory (Van de Ville et al., 2010; von Wegner et al., 2016).

We recently used an information-theoretical method to show that microstate sequences display another feature, namely oscillatory or periodic properties (von Wegner et al., 2017). In other words, microstate labels appeared stochastically, but with a preferred time interval. When a given microstate label, e.g. the map labelled 'A', was observed at a given time, there was a significantly increased probability to observe map 'A' again 50 ms, 100 ms, etc. later. Further analyses showed that these intervals correlated significantly with the dominant alpha frequencies of the studied individuals. In particular, microstates recurred with twice the alpha frequency. As the microstate label at each time point was selected by maximum similarity with the current EEG topography, we concluded that spatial patterns of resting-state alpha oscillations showed temporal periodicity (von Wegner et al., 2017).

The main goal of the present study was to identify the origin of these periodicities. The microstate procedure can be interpreted as a form of dimensionality reduction algorithm whereby the spatial information of a continuous EEG data set is massively compressed. To track the origin of microstate periodicity, we started our analysis at the very beginning of the procedure, at the level of continuous EEG sensor data. By that approach, we aimed to overcome the limitations implied by only considering EEG topographies at local maxima of the global field power (GFP, standard deviation of all voltage values across all EEG channels). Two recent articles provided a critical view on the winner-take-all approach used in microstate fitting and emphasized the continuous nature of the EEG dynamics that underlie microstate sequences (Mishra et al., 2020; Shaw et al., 2019). Both studies raised the issue of relevant EEG dynamics between GFP peaks which may not be represented adequately by the microstate approach.

Classical works (Lehmann et al., 1987) and recent advances using EEG source reconstruction algorithms (Milz et al., 2017) showed that microstates are mostly associated with alpha-band activity. For this reason, and due to the fact that the concept of phase is only well defined for narrow frequency bands (Huang et al., 1998), the present analysis focuses on the 8–12 Hz alpha range, the dominant EEG spectral peak in wakeful rest (Schomer and da Silva, 2011). Since EEG data at the sensor level is composed of amplitude-modulated oscillations with a dominant frequency, we studied the EEG's Hilbert transform which splits this class of signals into two components without information loss, the components being the (analytic) amplitude and the (analytic) phase.

Apart from examining the origin of microstate periodicity, we were motivated by the question if the phase of resting-state alpha oscillations forms spatial patterns. The phase component of cortical oscillations has received increasing attention as the carrier of biological information between neuronal populations such as different cortical areas, or the cortex and subcortical nuclei (Arenas et al., 2008; Masquelier et al., 2009).

Studies suggesting a specific biological role of the oscillatory phase involve alpha oscillations (Palva and Palva, 2011) as well as other EEG frequency bands (Vidaurre et al., 2018). Also, the general theory of non-linear oscillators and complex dynamical systems emphasizes the role of phase dynamics in coupling and information transfer (Pikovsky et al., 2001).

Finally, microstates have been discussed in the context of critical dynamics in the resting-state brain Van de Ville et al. (2010), to which amplitude and phase dynamics of EEG oscillations may contribute separately (Daffertshofer et al., 2018).

This set of questions motivated us to study the relation between microstates and alpha amplitude/phase patterns in more detail. In the following, we try to answer some of these questions by comparison of continuous EEG data and discrete microstate sequences derived from alpha oscillations, the analytic alpha amplitude and the analytic alpha phase.

The presentation is organized as follows. We examine the spatial properties of resting-state alpha oscillations as seen through the Hilbert transform. The visual identification of certain periodic phase patterns (phase rotors) is complemented by a quantitative description of geometrical invariants (singularities) that allow the automatic detection and quantification of these patterns. We then show that periodic phase patterns coincide with periodic microstate motifs involving all four classical microstate geometries (Koenig et al., 2002). Using time-lagged mutual information, we examine to which extent the analytic amplitude and phase contribute to microstate periodicity in a sample of 23 healthy subjects. Finally, we show that our results can be reproduced in a simple computational model of coupled non-linear oscillators with a supercritical Hopf bifurcation as their central feature. We conclude with a discussion of the results within the broader context of spatio-temporal EEG patterns and critical brain dynamics.

2. Material and methods

2.1. Experimental data

We analyzed $n = 23$ EEG recordings from right-handed healthy subjects (mean age: 23 yrs, range: 19–31, 9 males). All recordings were acquired in an eyes-closed resting-state condition. All data segments had a length of 120 s and were selected to be free of movement and electrode artefacts, and to show clear posterior alpha activity without signs of drowsiness or sleep. Written informed consent was obtained from all subjects and the study was approved by the ethics committee of the Goethe University, Frankfurt, Germany (reference number 305/07).

2.2. EEG signal processing

All data sets were recorded with a 30 channel EEG setup, using flexible EEG caps matched to the individual head size and using the standard 10–20 electrode configuration. The initial sampling rate was 5 kHz, and the data were re-referenced to the average reference as recommended for microstate analysis (Murray et al., 2008) and down-sampled to 250 Hz. Band-pass filters were obtained as zero-phase, 6th order Butterworth coefficients, resulting in a transfer function slope of 24 dB/octave. The alpha frequency band was obtained from 8 to 12 Hz band-pass filtering. We verified that the phase response in the alpha range was identical to that of a linear phase finite impulse response filter. As in our previous publications, the sampled EEG topography was interpolated and projected to a planar and regular 128×128 grid using cubic Clough-Tocher interpolation (von Wegner et al., 2018; von Wegner and Laufs, 2018; von Wegner et al., 2017).

2.3. Amplitude-phase decomposition

To separate amplitude and phase dynamics of alpha oscillations, the Hilbert transform was applied to band-pass filtered EEG signals. In the following, alpha frequency band filtered data will be denoted $\alpha(\mathbf{r}, t)$,

where \mathbf{r} denotes 2D spatial coordinates and t is time. The Hilbert transform of a signal $f(s)$ is commonly written as an integral transform

$$\tilde{f}(t) = \text{PV} \frac{1}{\pi} \int_{-\infty}^{+\infty} \frac{f(s)}{t-s} ds \quad (1)$$

where PV indicates the Cauchy principal value of the integral (Boas, 2006). In the frequency domain, the Hilbert transform only retains Fourier components of non-negative frequencies (Oppenheim and Schaffer, 1999).

A practical way to visualize the Hilbert transform of an oscillatory EEG signal is the following. Let the band-pass filtered alpha oscillation $\alpha(\mathbf{r}, t)$ and its Hilbert transform $\tilde{\alpha}(\mathbf{r}, t)$ be the real and imaginary parts of the complex-valued signal $z(\mathbf{r}, t) = \alpha(\mathbf{r}, t) + i\tilde{\alpha}(\mathbf{r}, t)$. The complex time series $z(\mathbf{r}, t)$ is called the analytic signal and has the same number of samples as the input signal. Each sample of the analytic signal is a vector in the 2D plane of complex numbers and the trajectory of the analytic signal describes a periodic motion around the origin. In polar coordinates, the amplitude or radius of the trajectory is the envelope of the oscillatory input and the angle between the real axis and the current Hilbert vector is the instantaneous phase. The analytic signal of the alpha oscillation in Cartesian and polar coordinates is thus given as:

$$\begin{aligned} z(\mathbf{r}, t) &= \alpha(\mathbf{r}, t) + i\tilde{\alpha}(\mathbf{r}, t) \\ &= A(\mathbf{r}, t) e^{i\phi(\mathbf{r}, t)} \end{aligned} \quad (2)$$

where $A(\mathbf{r}, t)$ denotes the analytic amplitude and $\phi(\mathbf{r}, t)$ the analytic phase. In our computations, phase values lie in the interval $[-\pi, +\pi]$, but other choices such as $\phi \in [0, 2\pi]$ are also consistent and do not affect the shown results in any way. For EEG data, the analytic amplitude and phase values were calculated from the spatially interpolated and band-pass filtered data sets using the discrete Hilbert transform as implemented in the open source SciPy package (Oppenheim and Schaffer, 1999).

2.4. Phase gradient and phase singularities

The phase gradient $\nabla\phi(\mathbf{r}, t)$ contains the discrete derivatives of the phase field along the two spatial dimensions. In discrete 2D coordinates, and omitting the time index for simplicity, the phase gradient at location $\mathbf{r} = (m, n)$ was computed as:

$$\nabla\phi_{m,n} = (\phi_{m+1,n} - \phi_{m,n}, \phi_{m,n+1} - \phi_{m,n}). \quad (3)$$

To identify phase singularities, the rotation (or curl) of the phase gradient field was calculated by virtue of Stokes' theorem as a contour integral along a closed path C around each 2D coordinate (pixel). Scaling the rotation of the gradient field by the factor $\frac{1}{2\pi}$ gives a quantity called the topological charge $\sigma(\mathbf{r}, t)$ (Bray, 1994; Bray et al., 2001; Bray and Wikswo, 2002). Thus, topological charge in continuous coordinates is defined as

$$\sigma(\mathbf{r}, t) = \frac{1}{2\pi} \oint_C \nabla\phi(\mathbf{r}, t) d\mathbf{l} \quad (4)$$

where $d\mathbf{l}$ is a differential line segment of the closed contour C . Numerically, we integrated along a square contour around each pixel (m, n) (Bray et al., 2001), i.e. along the set of pixels $\{(i, j) : \max(|i-m|, |j-n|) = 1\}$, following the mathematically positive (counterclockwise) direction. For a conservative, singularity-free gradient field, the rotation is zero and therefore, areas without phase singularities have a topological charge of zero ($\sigma = 0$). A singularity at the center of a rotor with mathematically positive (counterclockwise) orientation has a positive topological charge $\sigma > 0$, a negative (clockwise) rotation has $\sigma < 0$ (Bray and Wikswo, 2002; Qiao et al., 2009). As the phase can wind around the singularity $n = 1, 2, \dots$ times in positive or negative direction, the contour integral can have values of $\pm 2\pi n$, and the normalization constant $\frac{1}{2\pi}$ leads to (non-zero) integer values for the topological charge, $\sigma \in \mathbb{Z} \setminus \{0\}$. We only found rotors with a winding number of $n = 1$, i.e. theoretical values of $\sigma = \pm 1$. For experimental data,

the topological charge values are not exact integers but fluctuate around integer values due to the discretization and measurement noise. Here, we applied an empirically derived threshold of $|\sigma| > 0.85$ to identify phase singularities. In discrete coordinates, an individual singularity can cover more than one pixel and may be fragmented into non-connected points by the thresholding procedure. We therefore applied a morphological closing operator (Jähne, 2005) of 7×7 pixel square shape to the thresholded topological charge field. Therefore, phase singularities in all subsequent figures have a square shape. Overall, singularities are not difficult to detect automatically. As topological charge values away from singularities are zero, and all singularities produce topological charge peaks of the same absolute value, our results are stable even though the threshold is varied.

2.5. Microstate analysis

For each data set, four EEG microstates were computed using the spatial principal component analysis (PCA) method described in (von Wegner et al., 2018). Briefly, the spatial principal components of EEG data vectors taken at the local maxima of the global field power (GFP) time course were computed. The first four components were identified as microstate maps. The EEG data vector at each time point t was compared with each microstate map by computing the squared correlation coefficient between the two 30-component arrays. The microstate with the largest squared correlation coefficient determined the label of the microstate sequence L_t at time t , being the optimum representative of the current EEG topography ('winner-takes-all' strategy).

We decided to use the PCA-based method rather than the often used modified K-means algorithm (Pascual-Marqui et al., 1995) for three reasons: the PCA method is faster, it is not stochastic, i.e. it always gives the same set of microstates for a given EEG data set, and it has the same periodic properties as microstate sequences obtained with other methods (von Wegner et al., 2018).

We also computed microstate sequences for analytic amplitude and analytic phase signals using the same method. We respected the 2π periodicity of phase values $\phi \in [-\pi, +\pi]$ by using their complex representation $\exp(i\phi)$ during PCA and microstate fitting to the EEG data set.

As an alternative way to compress the information from the 30 EEG channels, we used temporal principal component analysis, and retained only the first component (tPCA₁) which explains the maximum amount of data variance. The tPCA₁ signal is a one-dimensional real-valued array with the same number of temporal samples as the original EEG data set.

Both, spatial and temporal PCA were implemented in Python and are available from our GitHub repository.

2.6. Autoinformation and autocorrelation analysis

Periodicity in microstate sequences was quantified via time-lagged mutual information (Kullback, 1959; von Wegner et al., 2017). Regarding the microstate label L_t at time t and the time-lagged label L_{t+k} as random variables with Shannon entropies $H(L_t)$, $H(L_{t+k})$ and conditional entropy $H(L_{t+k} | L_t)$, time-lagged mutual information for time lag k is defined as:

$$I(k) = H(L_{t+k}) - H(L_{t+k} | L_t). \quad (5)$$

In analogy to autocorrelation functions, we have previously used the term autoinformation function (AIF) for the collection of mutual information coefficients and we published the AIF code in the context of previous microstate-related articles (von Wegner et al., 2018; von Wegner and Laufs, 2018).

For real- and complex-valued signals x_t , we used the standard definition of autocorrelation coefficients r_{kk} at time lag k given by $r_{kk} = \mathbb{E}(x_t \bar{x}_{t+k})$ where $\mathbb{E}(\cdot)$ denotes statistical expectation and \bar{x}_{t+k} is the complex conjugate of x_{t+k} . To obtain the correct values for phase signals ϕ , these were represented as complex numbers in autocorrelation analyses.

2.7. Stuart-Landau oscillator lattice

Stuart-Landau oscillators represent the mathematical normal form of the supercritical Andronov-Hopf bifurcation (Kuznetsov, 2004), a common generating mechanism of non-linear oscillations. Using real-valued variables, the system can be written as a pair of differential equations, alternatively, the two real variables can be combined into a single complex number. We will here use the latter approach which directly compares to the complex EEG representation introduced via the Hilbert transform above (Eq. (2)). The dynamics of a single oscillator can be written as a differential equation:

$$\dot{z}_t = (\mu + i)z_t - z_t|z_t|^2 + \rho\xi_t \quad (6)$$

where \dot{z}_t denotes the time derivative of the complex variable $z \in \mathbb{C}$, and i is the imaginary unit. The variable z corresponds to the complex EEG representation introduced above. Eq. (6) is a stochastic differential equation (SDE) that contains a noise term $\rho\xi_t$, where ρ is the real-valued noise intensity and $\xi_t = \xi_t^{Re} + i\xi_t^{Im}$ are mutually independent complex-valued Gaussian random variables, i.e. $\xi_t^{Re}, \xi_t^{Im} \sim \mathcal{N}(0, 1)$ and $\langle \xi_s^{Re} \xi_t^{Re} \rangle = \langle \xi_s^{Im} \xi_t^{Im} \rangle = \langle \xi_s^{Re} \xi_t^{Im} \rangle = \delta(t - s)$. In this paper, the noise intensity was held constant at $\rho = 0.1$. The real-valued parameter μ defines the bifurcation point ($\mu = 0$) and controls the onset of oscillations. The supercritical Andronov-Hopf bifurcation is defined by the following properties:

- For $\mu < 0$, the system has a single stable fixed point $z_t = 0$
- At the bifurcation, $\mu = 0$, the fixed point vanishes and for
- $\mu > 0$, the system has a stable limit cycle $z_t = A \exp(it)$ with radius $A = \sqrt{\mu}$ and frequency $\omega = 1$, i.e. cycle length $T = 2\pi$

For details, we refer the reader to the extended literature on bifurcation theory, e.g. (Kuznetsov, 2004).

The spatial dimension is introduced by arranging $N = 64 \times 64$ oscillators on a discrete square lattice and coupling the elements diffusively:

$$\dot{z}(\mathbf{r}, t) = (\mu + i)z(\mathbf{r}, t) - z(\mathbf{r}, t)|z(\mathbf{r}, t)|^2 + \rho\xi_t + \Delta z(\mathbf{r}, t) \quad (7)$$

where \mathbf{r} is the spatial variable (two discrete indices in the lattice case) and Δ is the discrete Laplace operator that implements the coupling between neighbouring oscillators. For the discrete lattice case, we implemented the Laplace operator as:

$$\Delta z(\mathbf{r}, t) = \sum_{\mathbf{q}, d(\mathbf{r}, \mathbf{q})=1} (z(\mathbf{q}, t) - z(\mathbf{r}, t)). \quad (8)$$

The value of the Laplacian at the spatial location $\mathbf{r} = (i, j)$ is the sum over the differences $z(\mathbf{q}, t) - z(\mathbf{r}, t)$, where \mathbf{q} ranges over the nearest neighbours of \mathbf{r} , i.e. locations within unit distance ($d(\mathbf{r}, \mathbf{q}) = 1$). Explicitly, the neighbour set of $\mathbf{r} = (i, j)$ is $\{(i-1, j), (i+1, j), (i, j-1), (i, j+1)\}$.

We interpreted the SDE in the Itô sense and numerically integrated the system using the Euler-Maruyama scheme with a time step of $dt = 0.01$ (Gardiner, 2004; Kloeden and Platen, 1992). Each simulation run was allowed to equilibrate for 25000 time steps before recording 25000 iterations for analysis. We then down-sampled in time by a factor of 25 to obtain the same number of samples per oscillation cycle as for the EEG, i.e. approximately 25 samples per cycle (10 Hz alpha rhythm at 250 Hz sampling rate). The higher sampling rate ($dt = 0.01$) was used to assure stability of the numerical solution to Eq. (7), and down-sampling was applied to allow direct comparison between experimental and model data, excluding subtle differences introduced by different sampling rates. The band-pass filter and Hilbert transform parameters for the simulated oscillator data were identical to those of the EEG recordings, relative to the Nyquist frequency. Microstates for model lattices were computed by imitating the EEG sampling procedure. To achieve this, we selected 30 evenly spaced lattice sites and then applied the same procedure that is detailed in the Microstate analysis subsection.

3. Results

3.1. Amplitude-phase decomposition in time and space

The basic procedure used to process EEG data and to characterize spatio-temporal patterns is illustrated in Fig. 1. Awake resting-state EEG data is characterized by amplitude-modulated oscillations in the 8–12 Hz (alpha) frequency band, with the largest amplitudes occurring over the (parieto-)occipital cortex. This idea is illustrated in Fig. 1A, where the signal recorded at the left occipital EEG electrode (O1, 1–30 Hz, gray trace) and the first component of a temporal principal component analysis (tPCA₁, black) of the whole EEG data set are shown. While the O1 signal represents an actually recorded sensor signal, the tPCA₁ signal acts like a single (virtual) channel summarizing the activity occurring at all 30 sensors. In accordance with our previous report, we observed that both the frequency content and the amplitude dynamics of both signals were similar (von Wegner et al., 2017). We show an exemplary tPCA₁ signal here because tPCA₁ time courses will be used in subsequent sections to corroborate results obtained from the microstate transform. Both methods achieve the same goal of compressing a multi-channel EEG signal into a one-dimensional signal by different computational means. While the microstate method yields a sequence of symbols taken from the alphabet of microstate labels (A, B, C, D), the tPCA₁ approach gives a time series of real numbers. Microstate sequences will be processed by information-theoretical methods whereas the tPCA₁ time series can be analyzed by standard signal processing methods.

Fig. 1 B shows that alpha frequencies are the main constituent of occipital EEG activity during rest. The left occipital O1 signal (1–30 Hz, gray, identical to the gray trace in A but with different amplitude scaling) and the alpha band-pass filtered signal (8–12 Hz, black) both show the amplitude-modulated oscillations that characterize task-free EEG activity.

Fig. 1 C summarizes the amplitude-phase decomposition of the alpha frequency band signal as obtained from the Hilbert transform. The occipital alpha oscillation (black line) is identical to the black trace in panel B. The analytic Hilbert amplitude (blue line) has the same scaling as the O1 signal. The analytic amplitude corresponds to the envelope of the underlying oscillation, smoothly connecting its local maxima. It is useful to keep this image in mind when moving to the spatial view of alpha dynamics. The analytic amplitude represents the magnitude or intensity of the alpha oscillation at a given moment. The analytic phase (green line) encodes the current position within the 10 Hz oscillatory cycle, i.e. the proximity to local maxima, minima or zero crossings. The phase signal uses the right-hand scale ranging from $-\pi$ to $+\pi$. It is important to note that the recurring discontinuities of the phase signal, i.e. the jumps from $+\pi$ to $-\pi$, only occur in the one-dimensional representation. The corresponding complex vector $\exp(i\phi)$ moves smoothly along the complex unit circle.

Fig. 1 D briefly summarizes the steps leading from the continuous EEG signal to microstates, the details have been reported numerous times in the literature. The global field power (GFP) time series (black line) describes the spatial standard deviation across all EEG electrodes at any given time and oscillates with twice the alpha frequency. EEG topographies from time points where the GFP time series has local maxima (blue dots) are collected and processed by a dimensionality reduction or clustering algorithm which outputs the representative microstate maps. The algorithm to extract microstates in this case was spatial principal component analysis (PCA).

Fig. 1 E–H show spatial patterns or topographies taken at the time point of the GFP peak indicated in D (red dot). All topographies in this report follow the geometry indicated in panel E (l=left, r=right, fr=frontal).

Fig. 1 E is the EEG microstate map that represents the actual alpha band topography which is shown in Fig. 1F. Both maps share the same general symmetry, representing the basic idea of the microstate algorithm. In this example, the best fitting microstate map has the label C,

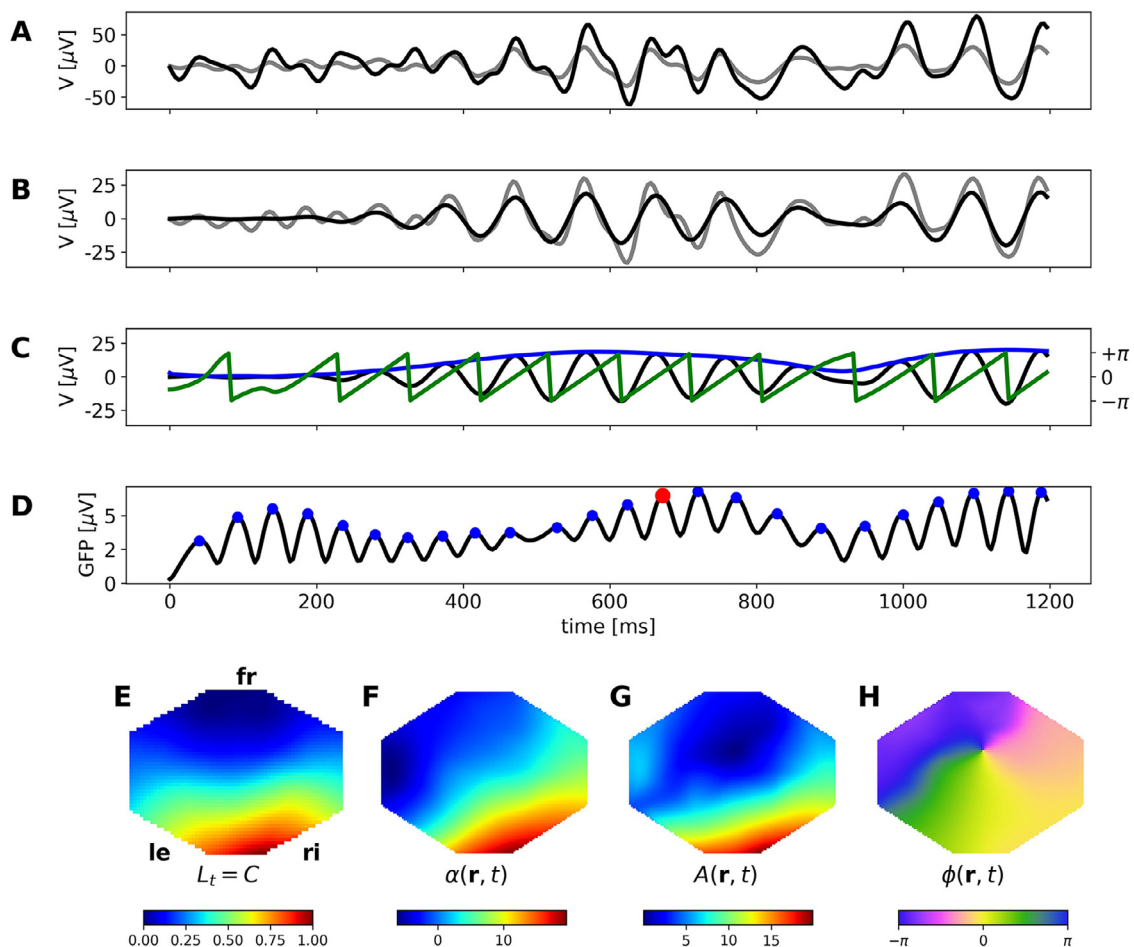


Fig. 1. Analytic amplitude-phase decomposition of oscillatory EEG signals. **A:** Both, the left occipital electrode signal (O1, gray) and the multi-channel activity as summarized by the first temporal principal component (tPCA₁, black) show an amplitude-modulated oscillation and similar temporal dynamics. **B:** The O1 electrode signal (gray) is dominated by the 8–12 Hz alpha frequency band component (black), showing that band-pass filtering only removes a small amount of data variance. **C:** The Hilbert transforms decomposes the O1 alpha oscillation (black) into two components, the analytic amplitude or envelope (blue), and the analytic phase (green), phase values are indicated by the right hand scale ($[-\pi, +\pi]$). Phase discontinuities only occur in the one-dimensional representation. **D:** The global field power (GFP, black) oscillates at approximately twice the alpha frequency, local maxima are indicated with blue dots. **E–H:** Spatial EEG topographies evaluated at an arbitrary GFP peak that is indicated by the red dot in **D**. All topographies have the orientation indicated in **E**: left (le), right (ri) and frontal (fr). **E:** Using standard labelling, the microstate at the GFP peak indicated in **D** has the label $L_t = C$ and represents the instantaneous EEG topography shown in **F**. **F:** Instantaneous topography of the alpha band oscillation $\alpha(\mathbf{r}, t)$ at the time point t . **G:** Instantaneous topography of the analytic amplitude $A(\mathbf{r}, t)$ at the same time point as **E**, **F** and **H**. The occipital amplitude maximum is characteristic for resting-state alpha oscillations. **H:** The topography of the analytic phase signal $\phi(\mathbf{r}, t)$ shows a single point in the fronto-central region where lines of constant phase (constant colour) coalesce and the value of the phase is undefined.

using standard microstate labelling conventions (Koenig et al., 2002). The amplitude and phase components of the analytic alpha signal are shown in **G**, **H**. The amplitude $A(\mathbf{r}, t)$ (**G**) shows that the maximum alpha magnitude occurs over occipital and parietal regions (red colours). The analytic phase $\phi(\mathbf{r}, t)$ (**H**) attains all values in the interval $[-\pi, +\pi]$ and varies smoothly at almost all locations of the scalp surface. An exception occurs at a fronto-central location where all phase values, or equivalently all colours coalesce. As a consequence, the phase value at this location cannot be defined unequivocally and these locations are termed phase singularities. However, around the singularities, the analytic phase changes continuously and shows a large-scale order. To avoid artificial discontinuities at boundaries where the (non-complex) phase value jumps from $+\pi$ to $-\pi$, phase maps are plotted with a circular colour map. It should be noted that the complex-valued EEG representation is continuous at these boundaries.

3.2. Phase gradient and phase singularities

Points of undefined phase as shown in **Fig. 1H** can be associated with rotating phase patterns. To visualize the temporal dynamics of phase

topographies, **Fig. 2A** shows four snapshots of the alpha phase over the course of approximately one alpha cycle, and with a spacing of 32 ms, or 8 frames with respect to the EEG sampling rate of 250 Hz. Using the phase colour scale shown on the right to track the phase field over the alpha cycle, a rotation of the phase pattern is observed. The two centers of rotation are located (i) close to the fronto-central midline, and (ii) further to the right (fronto-temporal area). Observing a fixed location during this rotation, we can observe that the local oscillators run through the full phase interval $[-\pi, +\pi]$, with the exception of the singular point near the center of the scalp. At the same time, the rotational pattern shows that the phase map away from the singularities shows a strong, large-scale ordering. Phase values are not scattered randomly across the scalp, but form a continuous field that maintains its symmetry during the shown rotation. At other time points, phase singularities can occur at different scalp locations and can move over time, as demonstrated further below. The locations shown in **Fig. 2** do not seem to play a privileged role and were chosen as an example. For better visualization, the data segment is animated in the supplemental file **Mov1_Fig_2**.

Fig. 2B quantifies the notions of phase rotation and phase singularity with analytical methods. The phase gradient (Eq. (3)) is visualized by

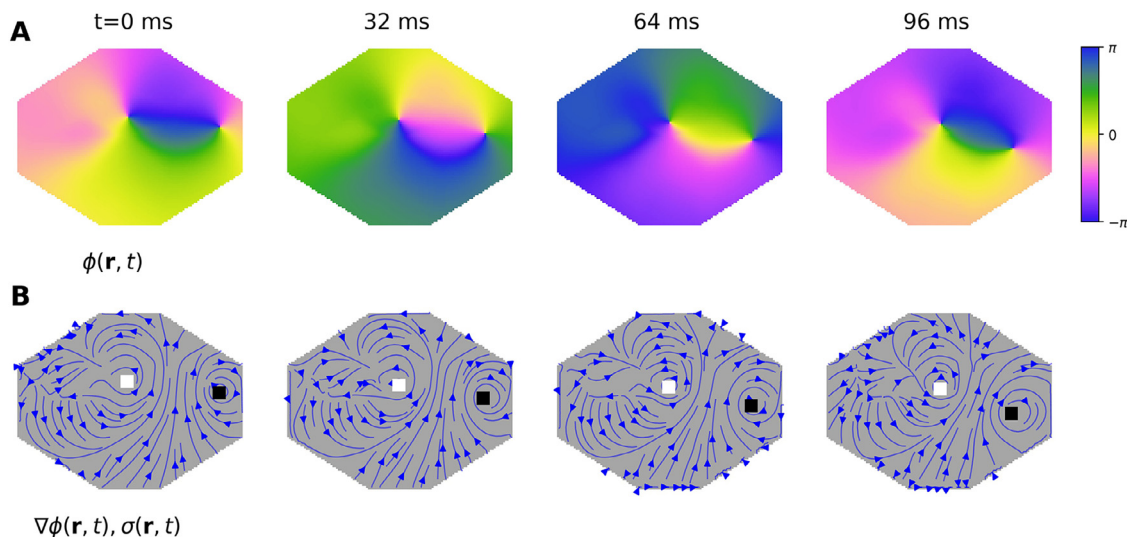


Fig. 2. Phase singularities, rotors and phase ordering. **A:** From left to right, phase topographies $\phi(\mathbf{r}, t)$ at four time points of an alpha oscillation cycle are shown. Visual analysis reveals two rotating phase patterns that complete approximately one rotational cycle over the 96 ms interval shown. There are two locations where the phase field is singular, i.e. where all phase values (all colours) coincide, one is found near the fronto-central midline, the other in the right fronto-temporal region. Following the colours along a closed loop encircling any one of the two points, it is noted that such a path visits all phase values in the $[-\pi, +\pi]$ interval continuously, demonstrating an ordering of the phase field around each singularity. Note the circular colour scale that avoids artificial discontinuities at $\pm\pi$ boundaries. **B:** The phase gradient $\nabla\phi(\mathbf{r}, t)$ (blue arrows) describes a counterclockwise rotation around the left singularity and a clockwise rotation around the right singularity at all time points. The counterclockwise rotation is summarized by the positive topological charge $\sigma(\mathbf{r}, t) = +1$ at the site of the left phase singularity (white square), whereas the clockwise gradient field rotation is encoded by a negative topological charge $\sigma(\mathbf{r}, t) = -1$ at the location of the phase rotor on the right (black square).

streamlines (blue arrows). These describe a counterclockwise (positive) rotation around the left phase singularity and a clockwise (negative) rotation around the singularity on the right. The topological charge, as defined in Eq. (4), is zero at all locations (gray background) except from the two phase singularities. In accordance with the orientation of the two rotors, we find $\sigma(\mathbf{r}, t) = +1$ for the positive rotation (white square), and $\sigma(\mathbf{r}, t) = -1$ for the negative rotation (black square). Thus, non-zero topological charge values localize phase singularities and the sign encodes the direction of rotation. The extent and square shape of the singularities as they appear in Fig. 2 are due to the image processing operators described in the Methods section. When inspecting the supplemental video animations, it is important to note that the sign of the rotor is defined by the direction of the phase gradient. This should not be confused with the rotation of the color values, which move in the opposite direction. At the boundary between $-\pi$ and $+\pi$ phase values (blue) for instance, the spatial gradient points from $+\pi$ to $-\pi$, corresponding to a phase increase along the positive direction on the complex unit circle. As the Hilbert transform only retains positive frequencies, phase values in the time domain jump from $+\pi$ to $-\pi$ (green line in Fig. 1C). By continuity, the color values rotate in the $-\pi$ -to- $+\pi$ direction, i.e. opposing the phase gradient vector.

3.3. Periodic microstate motifs and phase patterns

We here show that periodic microstate motifs are associated with periodic patterns of the corresponding alpha oscillation from which they were computed.

Fig. 3 illustrates the case of a periodic microstate pattern that occurs during a phase rotation around a phase singularity close to the vertex. In order to visualize the periodic dynamics that occur over approximately one and a half alpha cycles (144 ms), we chose an interval of 16 ms between the shown frames. In A, the microstate sequence L_t forms a periodic motif $(ACC)_n$ which is repeated three times during the shown time interval. The alpha oscillation topographies $\alpha(\mathbf{r}, t)$ represented by those microstates are displayed in B and indicate that the periodicity of the microstate labels is actually based on periodic EEG patterns, and not an artefact introduced by the microstate algorithm. Highly similar alpha

patterns with inverted polarity appear with a period of ≈ 50 ms (indicated by the asterisks at 0, 48, 96, 144 ms), while patterns of identical polarity are repeated with approximately the period of the alpha oscillation (e.g. 0 and 96 ms or 32 and 128 ms). At the same time, the analytic amplitude $A(\mathbf{r}, t)$ of the alpha oscillation, shown in C, remains almost constant over time, representing the classical alpha power distribution with an occipital maximum. The associated phase patterns $\phi(\mathbf{r}, t)$ are shown in D. While the location of the phase singularity remains almost immobile at the center of the map, the phase pattern completes a full rotation during the alpha oscillation cycle. The rotation velocity can be visually estimated by comparing the phase pattern observed in the first panel ($t = 0$ ms) and the distribution of phase values attained after one alpha cycle, in the time interval 96–112 ms. The phase gradient (blue streamlines) and the negative topological charge in E quantify the ongoing phase rotor and illustrate how efficiently the phase dynamics can be described and detected by these topological invariants. An animation of the data segment can be found in the supplemental file Mov2_Fig.3.

We made similar observations when other microstate maps were involved in periodic motifs. Fig. 4 illustrates the case of a periodic $(ABB)_n$ microstate motif, given a 16 ms frame interval. Again, the alpha oscillation (B) shows periodic behaviour with inverted polarities every 50 ms while retaining the same kind of spatial symmetry. Starting at $t = 0$ ms, alpha topographies with a diagonal symmetry corresponding to microstate type A are observed every 50 ms (asterisks indicate alpha half-cycles), while starting at $t = 16$ ms, the opposite diagonal pattern, i.e. microstate class B, is observed every 50 ms. Though the analytic amplitude in C changes during the 1.5 alpha cycles shown, the overall symmetry with a maximum over the right parieto-occipital areas is conserved. The phase patterns (D) in this example are organized by a pair of rotors over the right fronto-central region. Following the phase gradient patterns (E, blue streamlines) from left to right, the singularity further to the front and to the right rotates clockwise ($\sigma(\mathbf{r}, t) = -1$, black square), whereas the other one rotates in a counterclockwise manner ($\sigma(\mathbf{r}, t) = +1$, white square). The example also illustrates the fact that phase singularities are dynamic in space. In this case, both singularities move over time and their distance increases. The corresponding data segment is animated in the supplemental file Mov3_Fig.4.

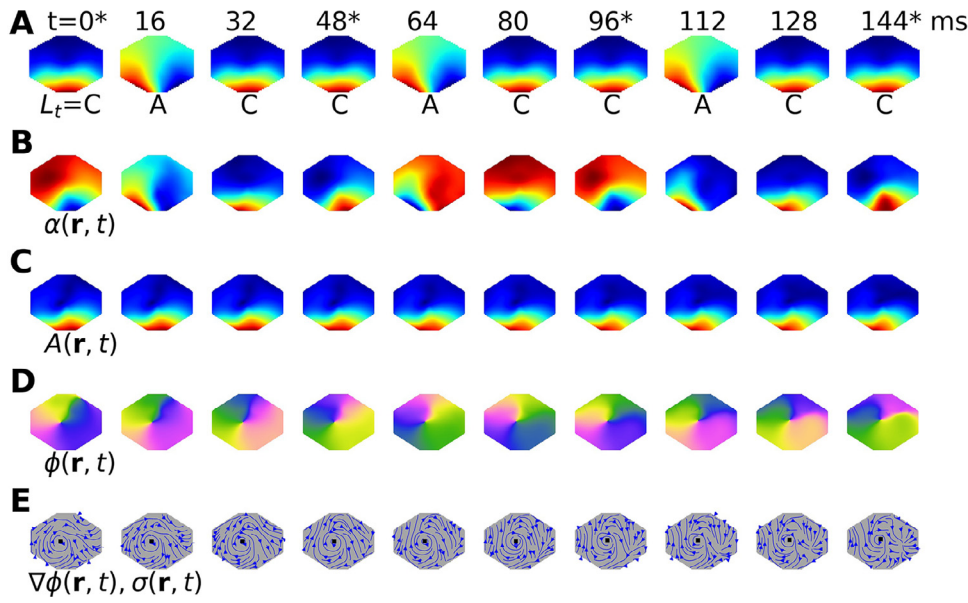


Fig. 3. Discrete and continuous EEG periodicity (I). **A:** At a spacing of $\Delta t = 16$ ms, the microstate sequence L_t shows a periodic $(ACC)_n$ motif. Time points are indicated above, and expected alpha half-cycles are indicated by asterisks at 0, 48, 96, 144 ms. **B:** The alpha band topographies $\alpha(r, t)$ represented by the microstate maps L_t shown in A. Almost identical topographies, but with inverted polarity, are observed at intervals close to half the alpha oscillation length, $\Delta t = 48$ ms. The microstate fitting procedure ignores EEG polarity. **C:** The analytic alpha amplitude $A(r, t)$ remains almost constant during the one and a half alpha cycles shown. **D:** The analytic phase $\phi(r, t)$ rotates around a singularity at the center of the phase map. As the alpha phase covers approximately 1.5 cycles, there are approximately 1.5 spatial rotations. **E:** The phase gradient $\nabla\phi(r, t)$ (blue streamlines) describes a constant clockwise rotation around a central singularity. The singularity is localized by the negative topological charge (black square) and the clockwise direction is defined by the negative sign $\sigma(r, t) = -1$.

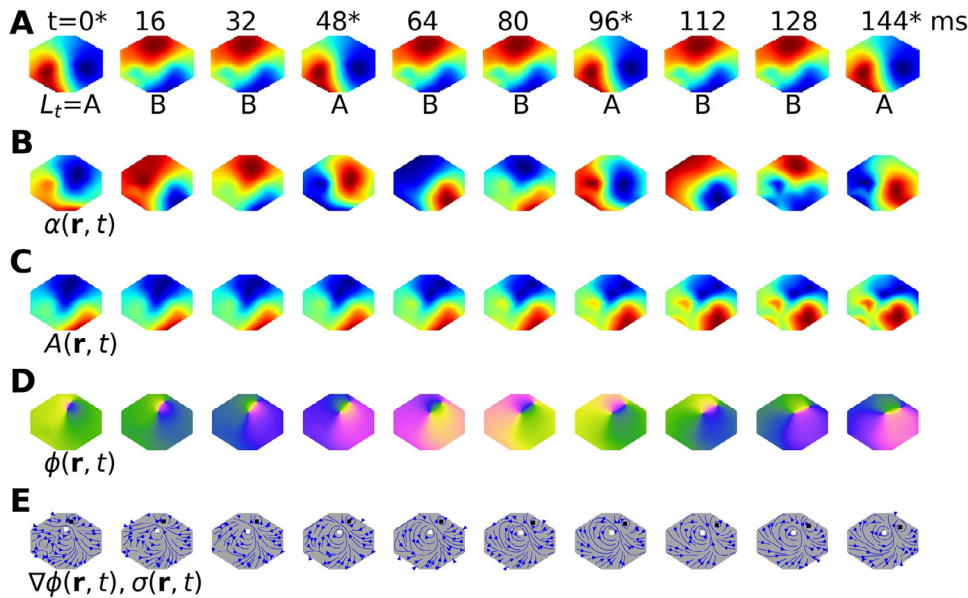


Fig. 4. Discrete and continuous EEG periodicity (II). **A:** At $\Delta t = 16$ ms, the microstate sequence L_t has a recurring $(ABB)_n$ motif, using standard microstate notation. Time points of expected alpha half-cycles are indicated by asterisks. **B:** The microstate maps A, B shown in A represent the concurrent alpha oscillation topographies $\alpha(r, t)$ with diagonal symmetry axes. At each half-cycle of the alpha oscillation ($\Delta t = 48$ ms) the alpha topographies show inverted polarity. **C:** The analytic amplitude pattern $A(r, t)$ changes in shape but retains the same diagonal symmetry and constant polarity. **D:** The analytic phase field $\phi(r, t)$ is organized by rotations around two singularities whose distance increases over time. **E:** The phase gradient $\nabla\phi(r, t)$ (blue streamlines) illustrates two phase rotors of opposite orientation. The location and orientation of the rotors is fully described by the values of the topological charge field. Clockwise: $\sigma(r, t) = -1$ (black square), counterclockwise $\sigma(r, t) = +1$ (white square).

Next, we analyzed a periodic microstate pattern involving the microstate maps C and D, leading to a periodic motif $(CCD)_n$ shown in Fig. 5A. The concurrent alpha topographies $\alpha(r, t)$ are shown in B and follow the same periodicity as discussed above. The alpha patterns in B show a high similarity with the associated microstates and invert their polarity approximately every 50 ms, i.e. each half-cycle of the alpha oscillation (asterisks in Fig. 5A). During the same period, the analytic alpha amplitude in C is very stable in terms of spatial pattern and polarity. The phase patterns in Fig. 5D show a pair of phase singularities emerging from a small fronto-central region and separating over time. Similar to Fig. 4, the two singularities rotate with opposite direction as quantified by the gradient field (blue streamlines) and the value of the topological charge $\sigma(r, t)$ in E. The centrally located singularity rotates counterclockwise, corresponding to a topological charge of $\sigma = +1$ (white square), and the right-posterior rotor has a clockwise orientation, equivalent to $\sigma = -1$ (black square). An animation of this data segment is provided in the supplemental file Mov4_Fig.5.

3.4. Spatio-temporal periodicity characterizes continuous and discrete EEG patterns

So far, we have established a close relationship between periodic microstate patterns and rotating phase patterns in continuous EEG data in three examples, using a spacing of $\Delta t = 16$ ms. This section extends and quantifies these observations over a broader range of time lags and using the original EEG sampling interval of 4 ms. Fig. 6 illustrates the relationship between periodic patterns in continuous EEG data and the discrete microstate representations using two independent approaches.

First, we used microstate sequences computed from the EEG alpha frequency band and computed their autoinformation functions (AIF) as specified in (von Wegner et al., 2018; von Wegner and Laufs, 2018; von Wegner et al., 2017). We then computed microstate sequences and their AIFs from the analytic alpha phase and analytic alpha amplitude signals obtained by the Hilbert transform.

In the second, microstate-independent approach, we processed alpha oscillations and their analytic amplitude and phase components by tem-

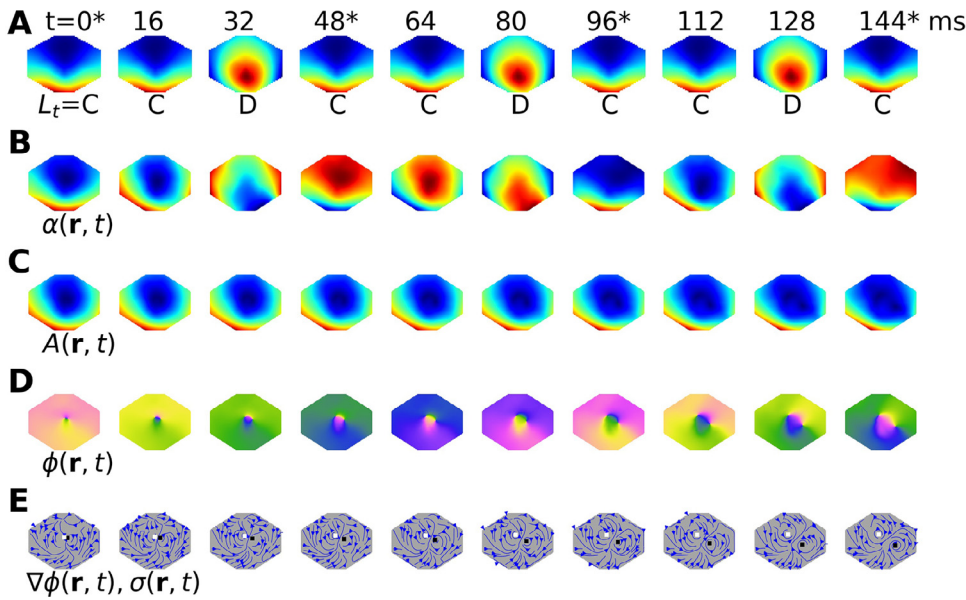


Fig. 5. Discrete and continuous EEG periodicity (III). **A:** This microstate sequence L_t has a periodic $(CCD)_n$ motif at $\Delta t = 16$ ms. Expected alpha half-cycles are indicated by asterisks. **B:** The concurrent alpha topographies $\alpha(r, t)$ show inverted polarities approximately every 48 ms. **C:** The analytic alpha amplitude $A(r, t)$ has almost constant shape and polarity during the 144 ms interval shown. **D:** The analytic phase field $\phi(r, t)$ rotates around a pair of singularities of slowly varying position and spatial distance. **E:** The phase gradient $\nabla\phi(r, t)$ (blue streamlines) and the topological charge map $\sigma(r, t)$ define a pair of opposite rotors, one with clockwise ($\sigma = -1$, black square) and the other with a counterclockwise ($\sigma = +1$, white square) orientation.

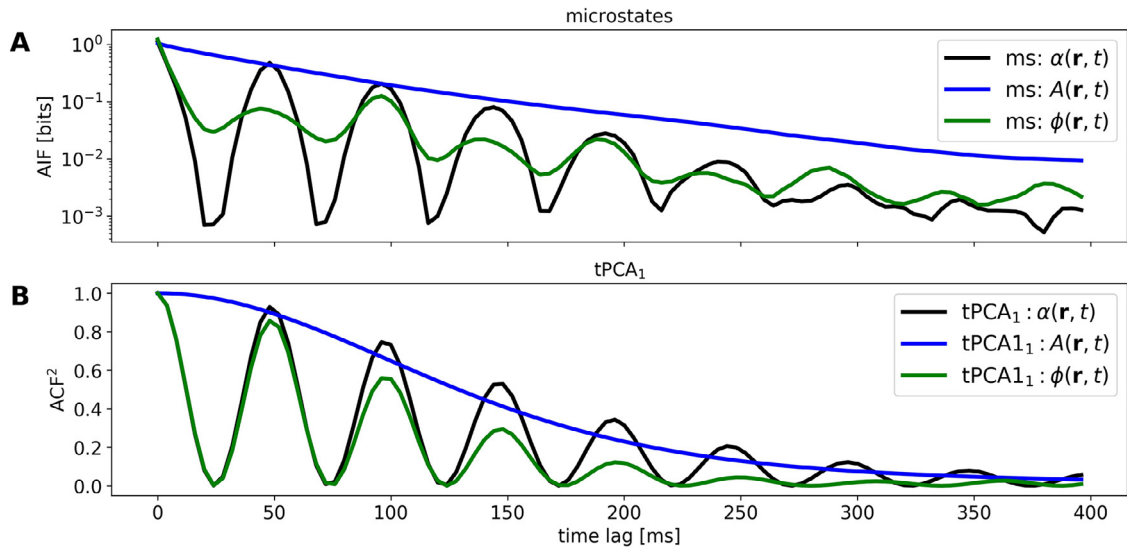


Fig. 6. Periodic spatial patterns for a single subject shown by two methods. **A:** The autoinformation function (AIF) of a single subject microstate sequence shows a clear periodicity at multiples of 50 ms, or half the alpha wavelength (black curve). The AIF of microstate sequences calculated from the analytic phase of the EEG signal (green) has a periodicity very similar to the classical microstate transform, whereas the AIF of microstate sequences computed from the analytic amplitude decays non-periodically (blue). **B:** Autocorrelation analysis for the first principal components (tPCA₁) of alpha oscillations, analytic alpha amplitude and phase. The squared autocorrelation function (ACF², black) for the tPCA₁ of the alpha band-pass data set shows a clear 50 ms periodicity (black line), representing periodic EEG topographies that invert their polarity at half the alpha wavelength. The tPCA₁ of the analytic phase has an ACF² with identical periodicity (green line), whereas the tPCA₁ of the analytic amplitude has non-periodic autocorrelations (blue line).

poral PCA rather than the microstate algorithm. For each of the three data sets, we only retained the first principal component (tPCA₁), i.e. the component that explains most of the data variance. Conceptually similar to the microstate approach, temporal PCA collapses all the spatial information into a one-dimensional signal. An exemplary tPCA₁ segment was shown in Fig. 1A. Since the tPCA₁ signals are real-valued, rather than a sequence of symbols, their periodicity could be quantified by classical autocorrelation analysis instead of using the information-theoretical method.

Fig. 6 A shows the autoinformation functions (AIFs) for a microstate sequence computed from the alpha frequency band of a single subject. The AIF shows a clear periodicity with a period of approximately 50 ms (black curve). The AIF of the microstate sequence computed from the analytic alpha phase (green) follows the same periodic pattern with equal

cycle length. The microstate sequence obtained from the analytic alpha amplitude, however, shows a monotonic decay without any peaks that would indicate periodicity.

This observation was corroborated by the second approach using temporal PCA. Fig. 6B shows the squared autocorrelation functions (ACF²) for the tPCA₁ signal of the alpha oscillation (black), the tPCA₁ of the analytic phase (green) and the tPCA₁ of the analytic amplitude (blue). The observed pattern is identical to Fig. 6A. Only the tPCA₁ components of the alpha oscillation (black line) and phase (blue line) signals have clearly periodic squared autocorrelation coefficients, with a minimum period of 50 ms. The amplitude-derived tPCA₁ autocorrelations (blue line), however, decay monotonously without periodic features. The period length of 50 ms is due to the squaring of the autocorrelation function and reflects the microstate fitting procedure which considers

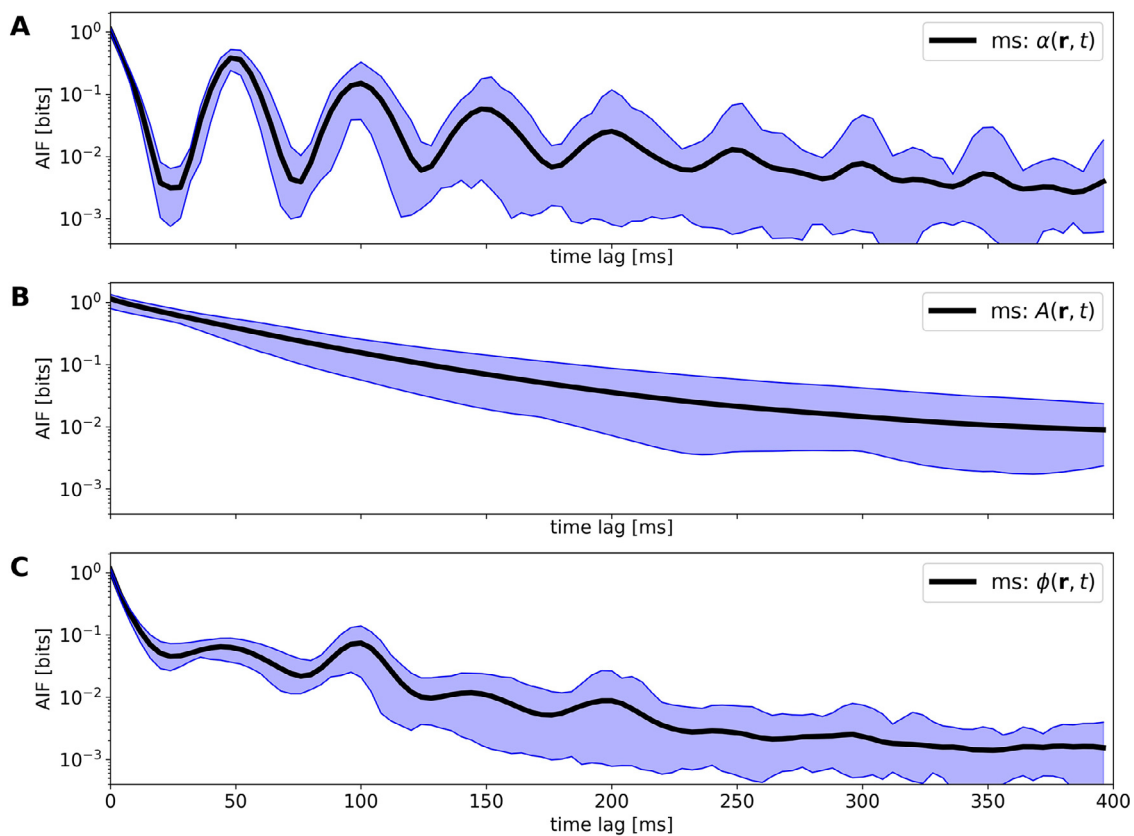


Fig. 7. Microstate periodicities in $n = 23$ resting-state recordings. **A:** EEG microstate sequences computed from the alpha frequency band show periodicities at multiples of 50 ms, consistent with resting-state oscillations centered around 10 Hz (or 100 ms) and polarity inversion over each half-cycle. **B:** Microstate sequences computed from the analytic alpha amplitude show slowly decaying AIFs without periodicity. **C:** Microstate sequences for the alpha phase follow the periodic pattern in **A**, with main peaks at multiples of 100 ms and minor peaks at multiples of 50 ms.

the squared correlation coefficient to measure similarity between EEG topographies and microstate maps.

Fig. 7 follows the logic of Fig. 6A and shows the group results across our sample of $n = 23$ healthy subjects in a resting-state condition. For better visibility, the AIFs for alpha oscillation microstates (A), analytic alpha amplitude microstates (B) and analytic phase microstates (C) are presented separately. Mean AIF coefficients are shown in black, the 95% confidence intervals as blue-shaded areas. Fig. 7A shows that the periodic AIF pattern presented in Fig. 6A is stable across the sample, i.e. microstates reliably occur with a periodicity of 50 ms. The highest AIF peaks are located at time lags of 50 and 100 ms, with subsequent peaks showing a marked decrease in amplitude due to the stochastic nature of microstate dynamics and due to averaging across subjects. For microstates computed from analytic alpha amplitudes, Fig. 7B shows no signs of periodic microstate recurrence. The mean AIF rather shows a slow and monotonous decay across the analyzed time lags up to 400 ms. None of the individual AIFs had periodic peaks either. We concluded that spatial patterns of the analytic alpha amplitude show no periodic pattern in time, for the time scales studied. Fig. 7C shows that alpha phase microstates have periodic properties. The mean AIF shows two clear peaks at time lags of 100 ms and 200 ms, with minor elevations at 50 ms, and possibly at 150 ms.

The supplementary file contains a statistical characterization of the different microstate maps computed from full bandwidth (1–30 Hz) data, alpha band-pass filtered data, and analytic amplitude and phase data. GFP properties and explained variance metrics are reported in Table S1, and S2 contains descriptors of the microstate probability distribution and the matrix of transition probabilities, in a microstate label-independent way. Overall, we did not find large deviations from the classical full bandwidth microstate transforms. Exemplary microstate

maps from alpha band, analytic amplitude and phase data sets for one subject are illustrated in Fig. S1.

3.5. A coupled oscillator model of critical phase pattern formation

Fig. 8 aims at reproducing the results obtained for experimental EEG data in the Stuart-Landau lattice model. All results shown here refer to a lattice model of size 64×64 with diffusive coupling and constant noise level ($\rho = 0.1$, see Methods). Fig. 8A and B show snapshots of the analytic phase of two different lattice simulations in which each oscillator undergoes an Andronov-Hopf bifurcation when the control parameter μ changes from negative to positive values. For $\mu = -0.5$, both simulations do not produce coherent phase patterns. Close to the bifurcation, at $\mu = -0.1$, both simulations show a spatial ordering of the phase, which becomes clearer at $\mu = 0$, showing a single phase singularity at the center of the lattice for simulation A, and a pair of phase singularities with opposite orientation in B. Going from $\mu = 0$ to $\mu = 0.5$, the spatial symmetry of both simulations remains unaltered, but the described patterns become sharper. The only difference between the simulations shown in A and B are the random initial conditions and the stochastic differential contributions $\rho \xi_t$ in Eq. (6). This illustrates the fact that the number and location of phase singularities depends only on the stochastic elements of the model, not on the control parameter μ or geometric factors. Animations of the two simulations are provided as supplemental files Mov5_CSLE_S1 and Mov6_CSLE_S2, respectively.

Fig. 8 C and D illustrate the temporal dynamics of the systems shown in A, B for a random lattice site. In C, we observe that there are no oscillatory dynamics at $\mu = -0.5$, whereas close to the critical point ($\mu = -0.1$), a low-amplitude oscillation can be discerned towards the end of the data trace. As expected for an Andronov-Hopf bifurcation, clear oscillations

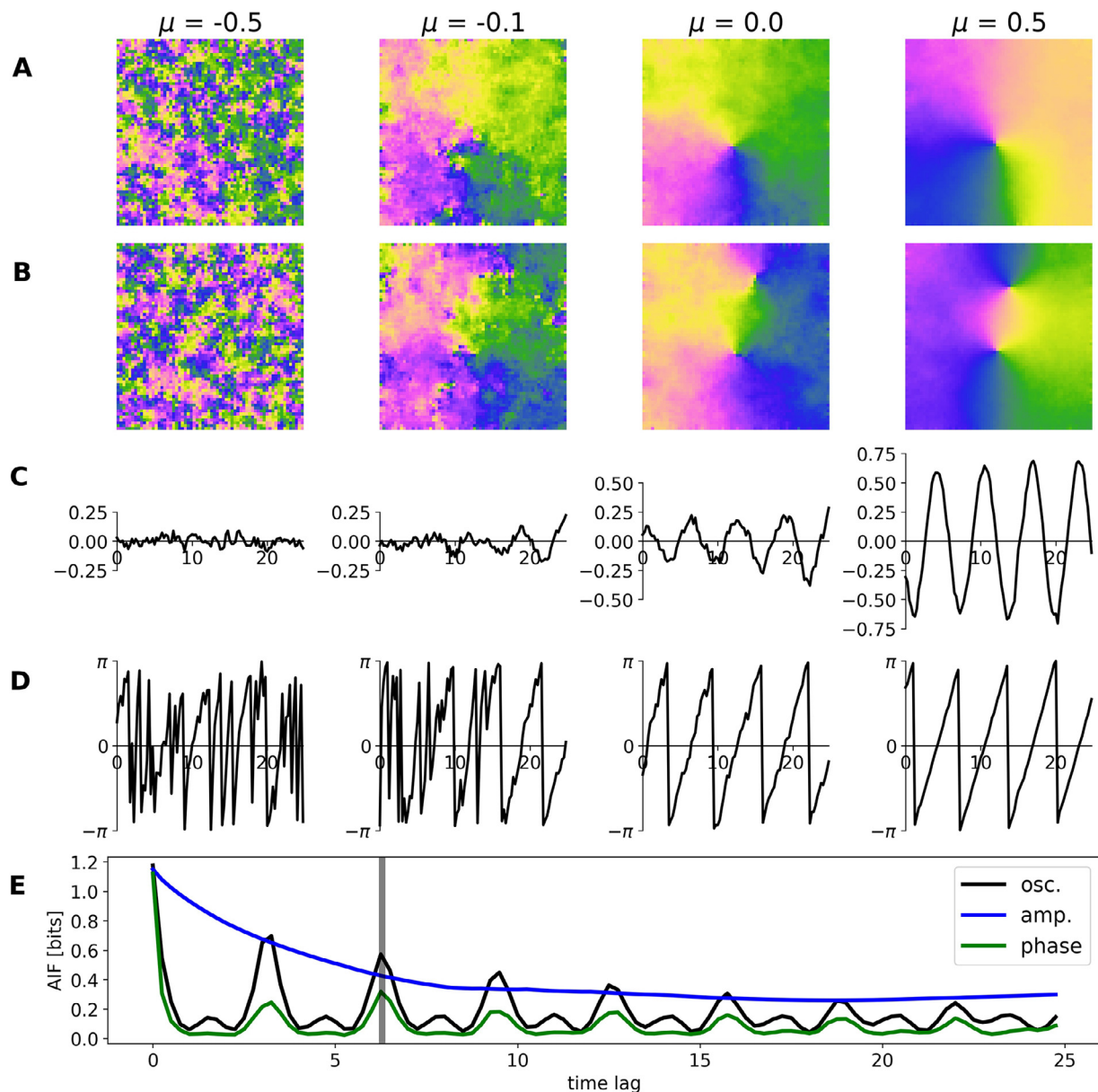


Fig. 8. Coupled oscillator model of periodic phase patterns. **A, B:** Spatial snapshots of phase patterns in coupled oscillator lattices for different control parameters μ . Below criticality ($\mu = -0.5$), the systems do not show clear spatial patterns. Close to the bifurcation point $\mu = 0.0$, phase singularities and associated phase rotors emerge (single rotor in **A**, a pair of rotors in **B**). **C:** Time courses for a single oscillator show random fluctuations below the bifurcation point ($\mu = -0.5$) and an onset of stable oscillatory behaviour close to ($\mu = -0.1$) and above the supercritical Hopf bifurcation point $\mu = 0$. **D:** Time courses for the phase of a single oscillator show the transition from random phase changes ($\mu = -0.5$) to stable periodic phase dynamics when the control parameter passes the Hopf bifurcation point $\mu = 0$. **E:** The microstate algorithm is used to analyze spatial patterns of the model system at the bifurcation point ($\mu = 0$). The band-pass filtered oscillation produces microstates with a periodic AIF (black line) and a period length of $T = 2\pi$ (vertical gray line). The same periodicity is found in the microstate AIF of the analytic phase signal (green line), but not for the AIF of analytic amplitude microstates (blue line).

with increasing amplitude are observed for $\mu = 0$ and $\mu = 0.5$. As the natural frequency of Stuart-Landau oscillators is $\omega = 2\pi f = 1$, the cycle length is $T = 2\pi \approx 6.28$. In terms of amplitude dynamics, it is observed that beyond the bifurcation point, single site oscillations have a constant, non-modulated amplitude. Similar dynamics are observed for the analytic phase shown in **D**. Below the bifurcation point the analytic phase varies randomly and the direction of rotation fluctuates ($\mu < 0$). Close to and beyond the bifurcation point $\mu = 0$, a stable rotation is represented by a steadily increasing phase, including jumps from $+\pi$ to $-\pi$ in the one-dimensional representation. Going from $\mu = 0$ to $\mu = 0.5$, the stochastic contributions markedly decrease and the phase dynamics at $\mu = 0.5$ appear practically deterministic. In general terms, temporal pattern formation goes in parallel with spatial phase pattern formation.

In **E**, a lattice simulation at the bifurcation point, i.e. with a constant parameter setting $\mu = 0$, is analyzed with the microstate approach. To this end, the time courses of 30 equally spaced lattice points were submitted to the same PCA-based microstate algorithm as used for 30 channel EEG data sets. This analysis was performed for the oscillatory model output as well as for the analytic amplitude and the analytic phase components. The corresponding autoinformation functions (AIF) for the model microstate sequences are shown with the same colours as used for EEG data. The oscillatory signal component, analogous to the alpha rhythm, has a periodic AIF (black line) with an oscillation length of 2π (vertical gray line), i.e. the cycle length of Stuart-Landau oscillators. In accordance with the phase rotors shown in **A** and **B**, phase microstates also have a periodic AIF (green line) with the same periodicity as the

oscillatory component. Microstates computed from the analytic amplitude lead to microstates with a slowly and monotonously decaying AIF (blue line). In summary, Stuart-Landau oscillator lattices at the bifurcation point of individual oscillators show microstate dynamics similar to EEG microstate data. The AIFs for control parameter settings μ far from the bifurcation point do not resemble experimental AIF forms and can be found in the supplementary file (Fig.).

4. Discussion

In the present work, we have established a connection between the previously described periodicity of EEG microstate sequences (von Wegner et al., 2017) and the continuous spatio-temporal patterns formed by alpha oscillations as measured by surface EEG. Our main results can be summarized as follows:

- The periodicity of EEG microstate sequences reflects periodic patterns of alpha oscillations in continuous space and time.
- The oscillatory properties of microstate sequences are coded by the analytic phase of alpha oscillations and not by the analytic amplitude.
- Over the course of 1–2 alpha cycles, the combination of quasi-static amplitude and periodic phase patterns characterize spontaneous EEG activity as transient standing wave patterns.
- Periodic phase patterns emerge from phase rotors, organized around a small number of phase singularities which are dynamic over time.
- Pattern formation in resting-state alpha activity can be modelled by near-critical coupled oscillator lattices close to an Andronov-Hopf bifurcation.

4.1. Temporal properties of microstate sequences

Resting-state microstate sequences have been modelled as Markov processes (Brodbeck et al., 2012; Gärtner et al., 2015) and via long-range correlated random walk models (Van de Ville et al., 2010). In a recent publication, we employed an information-theoretical approach and found intermediate results with regard to temporal correlations of microstate sequences (von Wegner et al., 2017). In particular, we found autocorrelations or memory effects that clearly exceeded effects that can be described by a probability transition matrix approach. However, these memory effects did not differ from a Markov model for time lags beyond 1000 ms. Our main finding was that the sequence of microstate labels showed oscillatory behaviour with a period of half the alpha rhythm cycle (50 ms).

The present results give further insight into the source of this periodic behaviour. Using the complex-valued EEG representation, it becomes clear that the discrete microstate sequence yields a discretized view of a continuous rotation of the alpha phase field. The actual phase rotors revealed by the Hilbert transform and visualized in Figs. 2–5 are not visible in the standard microstate map geometries as the latter are calculated from actual EEG time courses which contain both, the analytic amplitude and the analytic phase (see Eq. (2)). The number and location of these phase rotors vary over time and possibly contribute to the non-stationarity of microstate sequences previously described (von Wegner et al., 2017).

The phase field analysis provides the necessary link between spatial and temporal properties of alpha oscillations and explains how temporal periodicity at the single electrode level translates into periodic microstate sequences. The distinct patterns of the phase field are no simple corollary of the temporal oscillations at each electrode but provide insights into the coupling of alpha oscillations across the cortical surface. Actually, the phase of alpha oscillations at different scalp locations could be uncorrelated, and we would still observe an alpha peak in the spectral density of each EEG channel, but the sequence of spatial topographies would be uncorrelated and memory-less. At the same time, the aperiodic nature of the analytic amplitude topographies could not have been predicted. In contrast to our findings, oscillatory properties of microstate

sequences could have been caused by periodic amplitude patterns. However, in all our subjects, the periodicity of EEG topographies was fully contained in the phase signals and not in amplitude signals. The emerging picture of a standing wave, i.e. the combination of a static amplitude (or envelope) with a periodically changing phase will be further discussed in the following paragraph.

Our results also contribute to an ongoing discussion regarding the common approach to compute microstate maps only from EEG data vectors at global field power (GFP) peaks (Koenig et al., 2002). Two recent publications emphasized the continuous nature of EEG data and criticized the winner-take-all approach used in microstate fitting (Mishra et al., 2020; Shaw et al., 2019). Both reports observed that EEG topographies often fail to fully separate into distinct clusters and that at many time points, several maps with similar goodness-of-fit values compete. Comparing discrete and continuous approaches, our results may help to explain these observations. The rotating patterns we observed in our data show that the EEG topography does not switch from one pattern to the next, it rather undergoes a continuous transition. In Fig. 3, for instance, we observe that the actual EEG topography changes continuously and solely due to a constant flow of the phase values, while the amplitude remains constant. What changes instantaneously is the similarity measure of the EEG topography with the microstate maps A and C, whereas the topography itself changes continuously. Thus, irrespective of the number and the geometry of the used microstate maps, there will always be a transition interval during which subsequent microstate maps fit the topography equally well. Our results also suggest that the microstate approach does not miss any essentially different EEG patterns between GFP peaks because the underlying EEG pattern changes smoothly, not abruptly. Despite the massive data compression effected by the microstate approach, the essential alpha periodicity of the underlying EEG can be encoded by the limited set of $n = 4$ microstate maps. In the light of rotating phase patterns, the situation is similar to describing the positions of a spinning wheel by a small number of representative snapshots or linear combinations of those. Any set of snapshots of the rotation will fail to represent the true pattern most of the time, but the correct sequence of snapshots can compress the continuous process efficiently.

Understanding the relation between continuous EEG and discrete microstate dynamics may help to choose the right approach for a given question. Our hypothesis is that whenever two experimental conditions can be distinguished by their fundamental EEG periodicity, e.g. wake and sleep, the conditions will also be separable by the periodicity of their microstate sequences. This hypothesis will be the subject of forthcoming studies.

In summary, the phenomenon of microstate periodicity can only be understood from an integrated spatio-temporal perspective and thereby provides new insight into the general process of pattern formation in the brain.

4.2. Spatio-temporal pattern formation in the brain

In an early paper, Lehmann reported that alpha band topographies changed polarity every 50 ms, and observed that the maximum field values moved clockwise or counterclockwise between foci he termed preference areas (Lehmann, 1971). Actually, Lehmann's analysis of local field maxima and minima can be understood as a simple discretized phase analysis that can be extended to the full range of phase values using the Hilbert transform. The observation of periodically changing polarities lies at the core of the microstate algorithm (Lehmann et al., 1987) and led to the standard implementation of fitting microstate maps to EEG topographies using the squared correlation coefficient between spatial patterns, i.e. ignoring polarity (Pascual-Marqui et al., 1995). The present study reproduces these observations for continuous phase values and shows that the phase field is actually structured by a small number of phase rotors. As each oscillator runs through the $[-\pi, +\pi]$ interval during one alpha cycle, a perfectly stable phase rotor completes a

spatial cycle in one alpha cycle also. In other words, the colour distribution in phase topography plots repeats itself after one alpha cycle, i.e. after approximately 100 ms. Assuming nearly identical alpha frequencies across the cortex, this also means that the phase values after half an alpha cycle are shifted by a value of approximately π . Using Eq. (2), the value of the actual EEG oscillation is the real value of $A(\mathbf{r}, t) e^{i\phi(\mathbf{r}, t)}$, or $\alpha(\mathbf{r}, t) = A(\mathbf{r}, t) \cos \phi(\mathbf{r}, t)$. As $\cos(\phi) = -\cos(\phi \pm \pi)$, we find that $\alpha(\mathbf{r}, t + \frac{T}{2}) = -\alpha(\mathbf{r}, t)$, where T is the length of the alpha cycle and the amplitude distribution $A(\mathbf{r}, t)$ is arbitrary. In this model case of a perfect phase rotor, the microstate goodness-of-fit, which is computed as the squared correlation coefficient between $\alpha(\mathbf{r}, t)$ and each microstate map, is identical for t and for $t + \frac{T}{2}$. This short calculation shows that the classical microstate algorithm applied to systems of phase rotors is expected to yield periodicities of half the oscillation length. This corresponds exactly to the observations reported in (von Wegner et al., 2017) and to the results shown here, where phase rotors based on a 10 Hz oscillation produce microstate sequences with a 50 ms periodicity.

The general picture we deduce from our complex-valued EEG representation is that resting-state alpha oscillations transiently behave like standing wave patterns, which are characterized by ongoing oscillations with a stable envelope or amplitude distribution. Figs. 3–5 show that the analytic amplitude of alpha oscillations remains in a stable configuration while the actual alpha oscillation changes polarity several times. Standing wave patterns are in line with numerous predictions obtained from neural field models, e.g. (Coombes, 2005; Visser et al., 2017). Similar results were also obtained from models rooted in statistical mechanics (Ingber and Nunez, 2011) with conceptual links to higher cortical functions including theories of consciousness (Nunez and Srinivasan, 2006; Visser et al., 2017), reminiscent of the 'atoms of thought' hypothesis in microstate theory (Michel and Koenig, 2018). The functional role of phase patterns in general and of the alpha phase in particular has been discussed in (Ng et al., 2013) and (Palva and Palva, 2011). Earlier works discussed the shape of beta and gamma frequency band phase cones and their relation to stimulus processing (Freeman, 2004b). Interestingly, subsequent work by Freeman based on these results introduced the idea of metastable neural frames, conceptually very similar to the microstate approach (Freeman, 2005; Freeman and Holmes, 2005).

It should also be noted that the phenomenon of phase rotors does not necessarily have to occur in standing wave models and their experimental validation in task-free EEG constitutes a novel finding in itself. Recent computational experiments showed rotating activation patterns on the whole brain scale (Gabay et al., 2018; Roberts et al., 2019), and our results are the first experimental analog to these, to the best of our knowledge. Contrary to cardiac electrophysiology research, there are almost no accounts of rotor activities in the human brain, a notable exception being a study done with intracranial electrodes where rotors were observed in association with sleep spindles (Muller et al., 2016). Phase patterns similar to the ones shown here have also been reported for rat cortex (Huang et al., 2010). Spiral wave dynamics and phase rotors have been reported in a large number of complex systems in physics, chemistry and biology, as summarized in the monograph (Winfree, 2001). Our present study shows that these patterns are continuously produced by the resting brain and that they can be routinely recorded using simple surface EEG in healthy wake subjects.

Our study complements a large number of computational studies on pattern formation in the brain, providing insights into the kinds of patterns that actually occur during task-free activity in the alpha frequency range.

4.3. Implications for critical brain dynamics

The highly organized phase patterns found in experimental EEG data raise the question of their biophysical meaning and possible implications for brain function. A large number of publications has likened resting-state brain activity to a dynamical system near a bifurcation or a statistical system near a critical state (Daffertshofer et al., 2018; Linkenkaer-

Hansen et al., 2001; Tagliazucchi et al., 2013). Based on biophysical models, cortical activity is often modelled as a network of coupled nonlinear oscillators, in which each individual oscillator system has intrinsic bifurcation points (Deco et al., 2018; 2011; Valdes et al., 1999). The Stuart-Landau model analyzed here uses a spatially extended minimal model of a supercritical Andronov-Hopf bifurcation (Kuznetsov, 2004), the kind of bifurcation that occurs in many models of the cortical alpha rhythm (Aburn et al., 2012; Grimbert and Faugeras, 2006; Spiegel et al., 2010). Our results (Fig. 8) show that when the control parameter approaches the bifurcation point ($\mu = 0$), the model lattice produces the same phase patterns, including singularities and rotors, that we observed in experimental data. In the two examples shown, the model produces a single phase rotor and a pair of phase rotors of opposite sign, respectively. Location and number of phase rotors only depend on stochastic effects. The rotor patterns can be discerned around the bifurcation point and become much clearer for larger μ . Close to the bifurcation point, the model shows oscillations with clear amplitude modulation, whereas for large μ , the system has stationary phase rotors and stable oscillations with minimal amplitude modulation. In summary, resting-state EEG data shows properties similar to a system near a bifurcation, where alpha oscillations are strongly amplitude-modulated and phase rotors appear and disappear in varying number and location. Moreover, the analytic amplitude and phase dynamics at the critical point of the model are qualitatively similar to our experimental results, where periodic phase patterns and aperiodic amplitude patterns can be observed (Fig. 8 E). Thus, our results are in line with the general picture of near-critical resting-state dynamics. However, our results are based on the spatio-temporal feature of phase rotors, which has not been considered previously. As phase singularities can be detected at individual time stamps, this method does not suffer from problems associated with temporal non-stationarity often encountered with other measures of criticality (von Wegner et al., 2016).

4.4. Referencing and interpolation

Before we conclude, we will discuss some methodological issues. The first point concerns the choice of the EEG reference. Large parts of this article are concerned with the spatio-temporal properties of the analytic alpha phase. The chosen reference (common average) determines the phase values of the recorded oscillations as it sets the estimated zero level of the cortical potential. Therefore, in surface EEG, the phase of an oscillation is always an estimate based on the given reference. A change of reference is equivalent to adding a fixed value to each EEG sensor raw value, thus introducing an offset. Thus, the concrete phase pattern and the location of phase singularities do indeed depend on the used reference. However, the fact that phase singularities and phase rotors appear in resting state EEG does not depend on the chosen reference. Microstate analysis in particular has been introduced to obtain a reference-independent description of EEG dynamics as reviewed in (Murray et al., 2008). A common choice in microstate research is the average reference (Koenig et al., 1999; 2002; Lehmann et al., 2005; Milz et al., 2015; 2017), which we used in this article as well as in our previous works (Brodbeck et al., 2012; Kuhn et al., 2015; von Wegner et al., 2016; 2017). As our aim was to establish a connection between microstates and continuous EEG dynamics while staying within the standard microstate framework, the Hilbert transform was applied to the same average-referenced data sets from which microstates were computed. Possible future developments could involve regularized reference techniques as proposed in Hu et al. (2018) and Yao et al. (2019).

We also examined the 2D projection as a possible confounding factor in our analysis. We therefore examined the analytic amplitude and phase data in three dimensions, i.e. on the curved surface defined by the actual electrode positions of the EEG cap before projection onto the two-dimensional plane (Perrin et al., 1989). We consistently found that the phase patterns, including singularities and phase rotors, were not caused by projection but were also present on the curved surface. Given

our aim to analyze the dynamics of classical microstates and to facilitate visualization, we chose the planar two-dimensional EEG representation throughout the paper.

Band-pass filtering and B-spline interpolation, both linear operations on the data, cannot introduce phase rotors or more complex dynamics such as rotor pairs continuously moving across the scalp surface. These considerations were verified in filtered and unfiltered versions of the oscillator model. Other patterns we observed included pairs of singularities that emerge from a single location, or vice versa, move towards each other and coalesce in a single point (not shown here). This behaviour is well known in coupled oscillator theory and is routinely observed in experiments and models of other electrically active tissues such as cardiac muscle (Bray et al., 2001; Bray and Wikswo, 2002).

In summary, the choice of reference, 2D projection, interpolation or filtering in space or time cannot give rise to the observed phase patterns.

4.5. Limitations

Due to a number of free parameters and algorithmic choices inherent to microstate methodology, the present study could not cover the whole area of microstate research. However, our previous studies provide solid arguments why the here presented results are valid for variations of the microstate algorithm. The present study used the spatial PCA algorithm detailed in von Wegner et al. (2018) and retained $n=4$ microstates for each data set. We did not include variations of these two choices as our previous studies showed that microstate periodicity did not depend on the clustering method (von Wegner et al., 2018) or on the number of microstates (von Wegner et al., 2017). Specifically, we showed that microstate sequences had identical periodic signatures for five different microstate algorithms, including PCA (von Wegner et al., 2018). It must also be emphasized that we used 8–12 Hz band-pass filtered EEG data whereas most microstate studies used a frequency range that also include the beta, theta and delta frequency bands, e.g. 1–40 Hz (Britz et al., 2010; Brodbeck et al., 2012; von Wegner et al., 2016; 2017) or 2–20 Hz (Koenig et al., 2002; Lehmann et al., 2005). The analytic phase, however, is only well defined for narrow-band signals (Huang et al., 1998). If a narrow frequency band has to be chosen, both the resting-state condition and the microstate approach suggest the use of the alpha band, which on one hand is the dominant frequency in resting-state EEG, and on the other hand is the major contributor to microstate maps (Milz et al., 2015). Future studies can extend the current findings to other EEG frequency bands of interest. In the supplementary Fig. S1 we give an example showing that full bandwidth (1–30 Hz) microstates are almost identical to alpha (8–12 Hz) microstate maps.

5. Conclusion

The results presented in this paper yield new insights into the relations between continuous EEG oscillations and discrete microstate sequences. Apart from explaining the periodic nature of microstate sequences, our results provide a new view on critical pattern formation in the brain. We hope that our results contribute to the efforts to narrow the gap between continuous and frequency-based EEG analyses on the one hand, and microstate research on the other hand. Our findings provide insight into the process that transforms continuous EEG data into the discrete microstate representation by showing that the oscillatory properties of microstate sequences are completely rooted in the underlying EEG phase and not in the amplitude dynamics. This finding provides a possibly useful link between results on phase-coding in cognitive processes (Masquelier et al., 2009; Ng et al., 2013), particularly those involving alpha oscillations (Palva and Palva, 2011) and the emerging knowledge about microstates and cognition.

Finally, phase rotors should be further evaluated for their usefulness as biomarkers of physiological and pathological brain states.

Declaration of Competing Interest

The authors declare that the research was conducted in the absence of any commercial or financial relationships that could be construed as a potential conflict of interest.

CRedit authorship contribution statement

F. von Wegner: Conceptualization, Methodology, Software, Formal analysis, Visualization, Writing - original draft. **S. Bauer:** Validation, Visualization, Writing - original draft. **F. Rosenow:** Validation, Resources. **J. Triesch:** Formal analysis, Writing - original draft. **H. Laufs:** Conceptualization, Resources, Data curation, Project administration.

Acknowledgements

This work was funded by the Bundesministerium für Bildung und Forschung (grant 01 EV 0703) and by the LOEWE program CePTER.

Supplementary material

Supplementary material associated with this article can be found, in the online version, at [10.1016/j.neuroimage.2020.117372](https://doi.org/10.1016/j.neuroimage.2020.117372)

References

- Aburn, M.J., Holmes, C.A., Roberts, J.A., Boonstra, T.W., Breakspear, M., 2012. Critical fluctuations in cortical models near instability. *Front. Physiol.* 3, 331.
- Arenas, A., Díaz-Guilera, A., Kurths, J., Moreno, Y., Zhou, C., 2008. Synchronization in complex networks. *Phys. Rep.* 469, 93–153.
- Boas, M.L., 2006. *Mathematical Methods in the Physical Sciences*. John Wiley & Sons Inc.
- Bray, A.J., 1994. Theory of phase-ordering kinetics. *Adv. Phys.* 43 (3), 357–459.
- Bray, M.-A., Lin, S.-F., Aliev, R.R., Roth, B.J., Wikswo, J.P., 2001. Experimental and theoretical analysis of phase singularity dynamics in cardiac tissue. *J. Cardiovasc. Electrophysiol.* 12 (6), 716–722.
- Bray, M.-A., Wikswo, J.P., 2002. Use of Topological Charge to determine filament location and dynamics in a numerical model of scroll wave activity. *IEEE Trans. Biomed. Eng.* 49 (10), 1086–1093.
- Britz, J., Van De Ville, D., Michel, C.M., 2010. Bold correlates of eeg topography reveal rapid resting-state network dynamics. *NeuroImage* 52 (4), 1162–1170.
- Brodbeck, V., Kuhn, A., von Wegner, F., Morzelewski, A., Tagliazucchi, E., Borisov, S., Michel, C.M., Laufs, H., 2012. EEG microstates of wakefulness and NREM sleep. *NeuroImage* 62 (3), 2129–2139.
- Coombes, S., 2005. Waves, bumps, and patterns in neural field theories. *Biol. Cybern.* 93, 91–108.
- Daffertshofer, A., Ton, R., Kringelbach, M.L., Woolrich, M., Deco, G., 2018. Distinct criticality of phase and amplitude dynamics in the resting brain. *NeuroImage* 180, 442–447.
- Deco, G., Cabral, J., Saenger, V.M., Boly, M., Tagliazucchi, E., Laufs, H., Van Someren, E., Jobst, B., Stevner, A., Kringelbach, M.L., 2018. Perturbation of whole-brain dynamics in silico reveals mechanistic differences between brain states. *NeuroImage* 169, 45–56.
- Deco, G., Jirsa, V.K., McIntosh, A.R., 2011. Emerging concepts for the dynamical organization of resting-state activity in the brain. *Nat. Rev. Neurosci.* 12, 43–56.
- Freeman, W.J., 2004. Origin, structure, and role of background EEG activity. Part 1. Analytic amplitude. *Clin. Neurophysiol.* 115 (9), 2077–2088. doi:10.1016/j.clinph.2004.02.029.
- Freeman, W.J., 2004. Origin, structure, and role of background EEG activity. Part 2: Analytic Phase. *Clin. Neurophysiol.* 115, 2089–2107.
- Freeman, W.J., 2005. Origin, structure, and role of background EEG activity. Part 3. Neural frame classification. *Clin. Neurophysiol.* 116 (5), 1118–1129.
- Freeman, W.J., Holmes, M.D., 2005. Metastability, instability, and state transition in neocortex. *Neural Netw.* 18 (5–6), 497–504.
- Gabay, N.C., Babaie-Janvier, T., Robinson, P.A., 2018. Dynamics of cortical activity eigenmodes including standing, traveling and rotating waves. *Phys. Rev. E Stat. Nonlinear Soft Matter Phys.* 98, 042413.
- Gardiner, C., 2004. *Handbook of Stochastic Methods: for Physics, Chemistry and the Natural Sciences*, third ed. Springer.
- Gärtner, M., Brodbeck, V., Laufs, H., Schneider, G., 2015. A stochastic model for EEG microstate sequence analysis. *NeuroImage* 104, 199–208.
- Grimbert, F., Faugeras, O., 2006. Bifurcation analysis of Jansen's neural mass model. *Neural Comput.* 18 (12), 3052–3068. doi:10.1162/neco.2006.18.12.3052.
- Hu, S., Yao, D., Valdés-Sosa, P.A., 2018. Unified Bayesian estimator of EEG reference at infinity: rEST (Regularized Reference Electrode Standardization Technique). *Front. Neurosci.* 12, 297.
- Huang, N.E., Shen, Z., Long, S.R., Wu, M.C., Shih, H.H., Zheng, Q., Yen, N.-C., Tung, C.C., Liu, H.H., 1998. The empirical mode decomposition and the Hilbert spectrum for nonlinear and non-stationary time series. *Proc. R. Soc. Lond. A* 454, 903–995.

- Huang, X., Xu, W., Liang, J., Takagaki, K., Gao, X., Wu, J.-Y., 2010. Spiral wave dynamics in neocortex. *Neuron* 68, 978–990.
- Ingber, L., Nunez, P.L., 2011. Neocortical dynamics at multiple scales: EEG standing waves, statistical mechanics, and physical analogs. *Math. Biosci.* 229, 160–173.
- Jähne, B., 2005. *Digital Image Processing*, sixth ed. Springer, Heidelberg.
- Kloeden, P.E., Platen, E., 1992. *Numerical Solution of Stochastic Differential Equations*, second corrected printing Springer, Heidelberg.
- Koenig, T., Lehmann, D., Merlo, M.C., Kochi, K., Hell, D., Koukkou, M., 1999. A deviant EEG brain microstate in acute, neuroleptic-naïve schizophrenics at rest. *Eur. Arch. Psychiatry Clin. Neurosci.* 249 (4), 205–211.
- Koenig, T., Prichep, L., Lehmann, D., Sosa, P.V., Braeker, E., Kleinlogel, H., Isenhardt, R., John, E.R., 2002. Millisecond by millisecond, year by year: normative EEG microstates and developmental stages. *NeuroImage* 16 (1), 41–48.
- Kuhn, A., Brodbeck, V., Tagliazucchi, E., Morzelewski, A., von Wegner, F., Laufs, H., 2015. Narcoleptic patients show fragmented EEG-microstructure during early NREM sleep. *Brain Topogr.* 28 (4), 619–635.
- Kullback, S., 1959. *Information Theory and Statistics*. Dover Publications, Inc., Mineola, NY.
- Kuznetsov, Y.A., 2004. *Elements of Applied Bifurcation Theory*. Springer, New York.
- Lehmann, D., 1971. Multichannel topography of human alpha EEG fields. *Electroencephalogr. Clin. Neurophysiol.* 31, 439–449.
- Lehmann, D., Faber, P.L., Galderisi, S., Herrmann, W.M., Kinoshita, T., Koukkou, M., Mucci, A., Pascual-Marqui, R.D., Saito, N., Wackermann, J., Winterer, G., Koenig, T., 2005. EEG microstate duration and syntax in acute, medication-naïve, first-episode schizophrenia: a multi-center study. *Psychiatry Res.* 138, 141–156.
- Lehmann, D., Ozaki, H., Pal, I., 1987. EEG alpha map series: brain micro-states by space-oriented adaptive segmentation. *Electroencephalogr. Clin. Neurophysiol.* 67 (3), 271–288.
- Linkenkaer-Hansen, K., Nikouline, V.V., Palva, J.M., Ilmoniemi, R.J., 2001. Long-range temporal correlations and scaling behavior in human brain oscillations. *J. Neurosci.* 21 (4), 1370–1377.
- Masquelier, T., Hughes, E., Deco, G., Thorpe, S.J., 2009. Oscillations, phase-of-firing coding, and spike timing-dependent plasticity: an efficient learning scheme. *J. Neurosci.* 29 (43), 13484–13493.
- Michel, C.M., Koenig, T., 2018. EEG microstates as a tool for studying the temporal dynamics of whole-brain neuronal networks: a review. *NeuroImage* 180, 577–593.
- Milz, P., Faber, P.L., Lehmann, D., Koenig, T., Kochi, K., Pascual-Marqui, R.D., 2015. The functional significance of EEG microstates-associations with modalities of thinking. *NeuroImage* 125, 643–656.
- Milz, P., Pascual-Marqui, R.D., Achermann, P., Kochi, K., Faber, P.L., 2017. The EEG microstate topography is predominantly determined by intracortical sources in the alpha band. *NeuroImage* 162, 353–361.
- Mishra, A., Englitz, B., M.X., C., 2020. EEG microstates as a continuous phenomenon. *NeuroImage* 208, 116454.
- Muller, L., Piantoni, G., Koller, D., Cash, S.S., Halgren, E., Sejnowski, T.S., 2016. Rotating waves during human sleep spindles organize global patterns of activity that repeat precisely through the night. *eLife* 5, e17267.
- Murphy, M., Stickgold, R., Öngür, D., 2020. Electroencephalogram microstate abnormalities in early-course psychosis. *Biol. Psychiatry* 5, 35–44.
- Murray, M.M., Brunet, D., Michel, C.M., 2008. Topographic ERP analyses: a step-by-step tutorial review. *Brain Topogr.* 20 (4), 249–264.
- Musaeus, C.S., Nielsen, M.S., Høgh, P., 2019. Microstates as disease and progression markers in patients with mild cognitive impairment. *Front. Neurosci.* 13, 563.
- Musso, F., Brinkmeyer, J., Mobascher, A., Warbrick, T., Winterer, G., 2010. Spontaneous brain activity and EEG microstates: a novel EEG/fMRI analysis approach to explore resting-state networks. *NeuroImage* 52 (4), 1149–1161.
- Ng, B.S.W., Logothetis, N.K., Kayser, C., 2013. EEG phase patterns reflect the selectivity of neural firing. *Cereb. Cortex* 23, 389–398.
- Nishida, K., Morishima, Y., Yoshimura, M., Isotani, T., Irisawa, S., Jann, K., Dierks, T., Strik, W., Kinoshita, T., Koenig, T., 2013. EEG microstates associated with salience and frontoparietal networks in frontotemporal dementia, schizophrenia and Alzheimer's disease. *Clin. Neurophysiol.* 124 (6), 1106–1114.
- Nunez, P.L., Srinivasan, R., 2006. A theoretical basis for standing and traveling brain waves measured with human EEG with implications for an integrated consciousness.. *Clin. Neurophysiol.* 117 (11), 2424–2435.
- Oppenheim, A.V., Schaffer, R.W., 1999. *Discrete-Time Signal Processing*, second ed. Prentice Hall, Upper Saddle River, NJ.
- Palva, S., Palva, J.M., 2011. Functional roles of alpha-band phase synchronization in local and large-scale networks. *Front. Psychol.* 2, 204.
- Pascual-Marqui, R.D., Michel, C.M., Lehmann, D., 1995. Segmentation of brain electrical activity into microstates: model estimation and validation. *IEEE Trans. Biomed. Eng.* 42 (7), 658–665.
- Perrin, F., Pernier, J., Bertrand, J., Echallier, J.F., 1989. Spherical splines for scalp potential and current density mapping. *Electroencephalogr. Clin. Neurophysiol.* 72, 184–187.
- Pikovsky, A., Rosenblum, M., Kurths, J., 2001. *Synchronization. A Universal Concept in Nonlinear Sciences*. Cambridge University Press, Cambridge, UK.
- Qiao, Y., Wang, W., Minematsu, N., Liu, J., Takeda, M., Tang, X., 2009. A theory of phase singularities for image representation and its applications to object tracking and image matching. *IEEE Trans. Image Process.* 18 (10), 2153–2166.
- Roberts, J.A., Gollo, L.L., Abeysuriya, R.G., Roberts, G., Mitchell, P.B., Woolrich, M.W., Breakspear, M., 2019. Metastable brain waves. *Nat. Commun.* 10, 1056.
- Schiller, B., Koenig, T., Heinrichs, M., 2019. Oxytocin modulates the temporal dynamics of resting EEG networks. *Scientific Reports* 9, 13418.
- , 2011. In: Schomer, D.L., da Silva, F.H.L. (Eds.), *Niedermeyers Electroencephalography: Basic Principles, Clinical Applications, and Related Fields*, sixth ed.. Lippincott Williams & Wilkins.
- Shaw, S.B., Dhindsa, K., Reilly, J.P., Becker, S., 2019. Capturing the forest but missing the trees: microstates inadequate for characterizing shorter-scale EEG dynamics. *Neural Comput.* 31 (11), 2177–2211.
- Smailovic, U., Koenig, T., Laukka, E.J., Kalpouzos, G., Andersson, T., Winblad, B., Jelic, V., 2019. EEG time signature in Alzheimer's disease: functional brain networks falling apart. *NeuroImage* 24, 102046.
- Spiegler, A., Kiebel, S.J., Atay, F.M., Knsche, T.R., 2010. Bifurcation analysis of neural mass models: Impact of extrinsic inputs and dendritic time constants. *Neuroimage* 52 (3), 1041–1058. doi:10.1016/j.neuroimage.2009.12.081.
- Tagliazucchi, E., von Wegner, F., Morzelewski, A., Brodbeck, V., Jahnke, K., Laufs, H., 2013. Breakdown of long-range temporal dependence in default mode and attention networks during deep sleep. *Proc. Natl. Acad. Sci. USA* 110 (38), 15419–15424.
- Valdes, P.A., Jimenez, J.C., Riera, J., Biscay, R., Ozaki, T., 1999. Nonlinear EEG analysis based on a neural mass model. *Biol. Cybern.* 81, 415–424.
- Van de Ville, D., Britz, J., Michel, C.M., 2010. EEG microstate sequences in healthy humans at rest reveal scale-free dynamics. *Proc. Natl. Acad. Sci. USA* 107 (42), 18179–18184.
- Vidaurre, D., Hunt, L.T., Quinn, A.J., Hunt, B.A.E., Brookes, M.J., Nobre, A.C., Woolrich, M.W., 2018. Spontaneous cortical activity transiently organises into frequency specific phase-coupling networks. *Nat. Commun.* 9, 2987.
- Visser, S., Nicks, R., Faugeras, O., Coombes, S., 2017. Standing and travelling waves in a spherical brain model: the Nunez model revisited. *Physica D* 349, 27–45.
- von Wegner, F., Knaut, P., Laufs, H., 2018. EEG microstate sequences from different clustering algorithms are information-theoretically invariant. *Front. Comput. Neurosci.* 12, 30.
- von Wegner, F., Laufs, H., 2018. Information-theoretical analysis of EEG microstate sequences in Python. *Front. Neuroinform.* 12, 30.
- von Wegner, F., Tagliazucchi, E., Brodbeck, V., Laufs, H., 2016. Analytical and empirical fluctuation functions of the eeg microstate random walk - short-range vs. long-range correlations. *NeuroImage* 141, 442–451.
- von Wegner, F., Tagliazucchi, E., Laufs, H., 2017. Information-theoretical analysis of resting state eeg microstate sequences - non-Markovianity, non-stationarity and periodicities. *NeuroImage* 158, 99–111.
- Winfree, A.T., 2001. *The Geometry of Biological Time*, second ed. Springer, New York.
- Yao, D., Qin, Y., Hu, S., Dong, L., Bringas Vega, M.L., Valdés-Sosa, P.A., 2019. Which reference should we use for EEG and ERP practice? *Brain Topogr.* 32, 530–549.
- Yuan, H., Zotev, V., Phillips, R., Drevets, W.C., Bodurka, J., 2012. Spatiotemporal dynamics of the brain at rest—exploring EEG microstates as electrophysiological signatures of BOLD resting state networks. *NeuroImage* 60 (4), 2062–2072.
- Zappasodi, F., Perrucci, M.G., Saggino, A., Croce, P., Mercuri, P., Romanelli, R., Colom, R., Ebisch, S.J.H., 2019. Eeg microstates distinguish between cognitive components of fluid reasoning. *NeuroImage* 189, 560–573.